energies

MDPI

Article

Effects of Recombination Order on Open-Circuit Voltage Decay Measurements of Organic and Perovskite Solar Cells

Joachim Vollbrecht [1,*] **and Viktor V. Brus** [2,*]

[1] Soft Matter Physics Group, Institute of Physics and Astronomy, University of Potsdam, 14476 Potsdam-Golm, Germany
[2] Department of Physics, School of Sciences and Humanities, Nazarbayev University, Nur-Sultan 010000, Kazakhstan
* Correspondence: vollbrecht@uni-potsdam.de (J.V.); viktor.brus@nu.edu.kz (V.V.B.)

Abstract: Non-geminate recombination, as one of the most relevant loss mechanisms in organic and perovskite solar cells, deserves special attention in research efforts to further increase device performance. It can be subdivided into first, second, and third order processes, which can be elucidated by the effects that they have on the time-dependent open-circuit voltage decay. In this study, analytical expressions for the open-circuit voltage decay exhibiting one of the aforementioned recombination mechanisms were derived. It was possible to support the analytical models with experimental examples of three different solar cells, each of them dominated either by first (PBDBT:CETIC-4F), second (PM6:Y6), or third (irradiated $CH_3NH_3PbI_3$) order recombination. Furthermore, a simple approach to estimate the dominant recombination process was also introduced and tested on these examples. Moreover, limitations of the analytical models and the measurement technique itself were discussed.

Keywords: organic solar cells; perovskite solar cells; non-geminate recombination; recombination order; open-circuit voltage decay

check for updates

Citation: Vollbrecht, J.; Brus, V.V. Effects of Recombination Order on Open-Circuit Voltage Decay Measurements of Organic and Perovskite Solar Cells. *Energies* **2021**, *14*, 4800. https://doi.org/10.3390/en14164800

Academic Editor: Antonio Rosato

Received: 19 July 2021
Accepted: 4 August 2021
Published: 6 August 2021

Publisher's Note: MDPI stays neutral with regard to jurisdictional claims in published maps and institutional affiliations.

Copyright: © 2021 by the authors. Licensee MDPI, Basel, Switzerland. This article is an open access article distributed under the terms and conditions of the Creative Commons Attribution (CC BY) license (https://creativecommons.org/licenses/by/4.0/).

1. Introduction

In recent years, new types of devices based on organic or organic–inorganic hybrid semiconductors have emerged and garnered a lot of attention. More specifically, applications such as light-emitting diodes [1–4], field-effect transistors [5–8], solar cells [9–11], photodiodes [12–15], sensors [16,17], and other types of energy-harvesting devices [18–20] have been in the spotlight. Lately, a significant performance increase was observed specifically for solar cells, either through the use of perovskites or, more recently, through the advent of so-called non-fullerene, bulk-heterojunction organic solar cells [10,21]. As promising as these results are, further improvements are a prerequisite for these emerging technologies to take a foothold as a widespread commercial and industrial alternative to their inorganic counterparts [22–25].

One main aspect that needs to be further understood is the loss mechanisms that reduce the overall performance of these new types of solar cells. Apart from losses due to leakage currents within the device, potentially resulting from faulty active layers that contain pinholes, more fundamental loss mechanisms also need to be investigated in detail. Specifically non-geminate recombination, which is the recombination of free charge carriers originating from two different excitons, needs to be curtailed [26]. In general, the different non-geminate recombination mechanisms can be categorized by the relationship of the recombination rate $R(t)$ and the charge carrier density $n(t)$:

$$R(t) = \frac{\mathrm{d}n(t)}{\mathrm{d}t} = -k \cdot n(t)^{\beta}, \quad (1)$$

where k is the recombination coefficient, and β is the recombination order. First order recombination ($\beta = 1$) usually results from the presence of trap states deep within the band gap. It is also commonly known as Shockley–Read–Hall recombination [27]. Second order recombination ($\beta = 2$), otherwise known as band-to-band or bimolecular recombination, results from direct transitions [28]. Third order recombination ($\beta = 3$), or Auger recombination, usually only occurs under conditions with very high charge carrier densities that are neither relevant for perovskite nor organic solar cells under realistic operating conditions [29,30]. The only exception is surface trap-assisted recombination, where the combination of trap states and band bending results in (pseudo) third order processes (cf. Figure 1) [31,32]. In experiments, solar cells tend to exhibit combinations of the three aforementioned recombination mechanisms.

Several strategies to reduce the losses in organic solar cells have been presented in recent years. One of the first important aspects is to align the relevant energy levels of the active layer components and the transport layers, as well as provide enough energetic driving force to enable exciton splitting [33]. Moreover, blend morphology plays a crucial role in device performance and strategies such as solvent additives [34], solvent–water evaporation [35], solvent vapor annealing [36], thermal annealing [37], and the use of compatibilizers [38] have become standard procedures. Furthermore, factors such as the length of the donor polymers can also have a significant influence on device performance [39,40]. In addition, the right choice of transport layers [41] and device architecture [42] is important to mitigate losses at the interfaces.

Different types of techniques exist to qualitatively and/or quantitatively describe the non-geminate recombination mechanisms within solar cells. These can range from comparatively simple measurements under a steady state, such as light-intensity-dependent current density–voltage (J-V) characteristics, which can qualitatively be used to estimate the dominant non-geminate recombination mechanism [43,44], to more elaborate measurements that can yield quantitative values for the recombination coefficients k and charge carrier recombination lifetimes τ [45]. These include optoelectronic techniques such as impedance spectroscopy [46,47], transient photovoltage and transient photocurrent [48], open-circuit voltage decay (OCVD) [49,50] or purely optical techniques, such as photon-induced absorption spectroscopy [51].

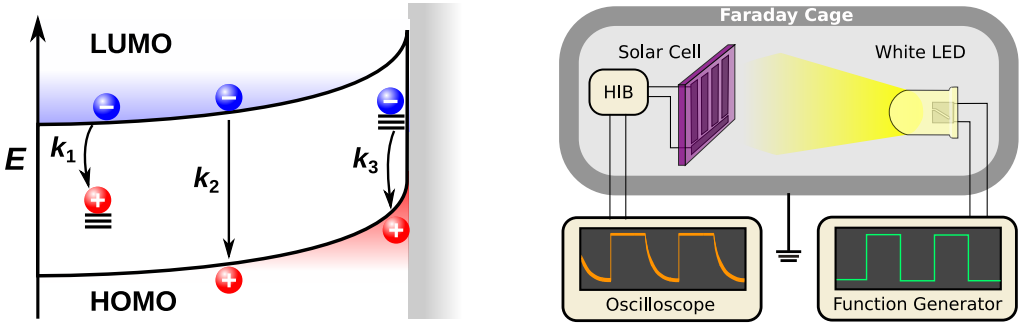

Figure 1. Schematic representation of first, second, and third order recombination processes, namely, Shockley–Read–Hall, bimolecular, and surface trap-assisted recombination and experimental setup to measure OCVD traces.

In this work, we show how OCVD can be employed to obtain relevant information with regard to the non-geminate recombination dynamics in organic or perovskite solar cells. First, the necessary analytical models to describe different types of recombination order are derived, and a fast, qualitative approach to estimate the dominating recombination mechanism from the first derivative is presented. Secondly, strategies to convert the time-dependent open-circuit voltage $V_{OC}(t)$ to the time-dependent charge carrier density $n(t)$ are discussed, specifically only by using OCVD and standard J-V measurements. Thirdly, the analytical models are tested with the experimental results of three types of

solar cells, each one dominated either by first, second, or third order recombination. Finally, limitations of the proposed analysis are also discussed in detail.

2. Materials and Methods

Three different types of solar cells were investigated as prime examples for devices dominated either by first, second, or third order recombination mechanisms, respectively. In the case of first order recombination, an organic bulk-heterojunction solar cell using PBDBT:CETIC-4F as active layer was selected, as this is a material combination that has been shown to be dominated by trap-assisted recombination in the bulk, which is a first order process [52]. An organic bulk-heterojunction solar cell based on PM6:Y6 as active layer was selected as an example for second order recombination dominating a device. The exceptional high performance of PM6:Y6 is also apparent in these measurements, as only the (unavoidable) losses due to band-to-band recombination are relevant [53]. Moreover, a proton-irradiated perovskite solar cell based on $CH_3NH_3PbI_3$ was used as an example for a device dominated by third order recombination processes; in this case, prolonged surface trap-assisted recombination [29]. It should be noted that it is quite challenging to find good examples of organic or perovskite solar cells that clearly exhibit third order recombination, since most devices will be subject to a combination of all three of these mechanisms, and third order recombination, in particular, rapidly loses its dominance with decreasing charge carrier density [29,31]. The specific details of the chemical structures, device architectures and fabrication procedures are listed in the respective literature [29,52,53].

The OCVD measurements were performed by keeping the tested devices under open-circuit conditions via a high impedance buffer (HIB). A fast switching light source, in this case a white LED connected to a function generator, was used to obtain photogenerated charge carriers in the tested solar cells. The time-dependent open-circuit voltage was monitored by an oscilloscope via the HIB, which then yielded the V_{OC}-t-traces that are used for the subsequent analysis (cf. Figure 1).

3. Results and Discussion

3.1. Analytical Expressions

The starting point of the analytical expressions that will be derived in this section is the equation describing the evolution of the open-circuit voltage in dependence of time $V_{OC}(t)$:

$$V_{OC}(t) = \frac{E_{CT}}{q} - \frac{2k_B T}{q} \ln\left(\frac{N_0}{n(t)}\right), \tag{2}$$

where q is the elementary charge, k_B is Boltzmann's constant, T is the absolute temperature, E_{CT} is the energy of the charge transfer state or alternatively the effective bandgap, N_0 is the effective density of states, and $n(t)$ is the time-dependent charge carrier density [54]. The derivation of Equation (2) is discussed in detail in Appendix A. The parameter that is most influential in the progression of $V_{OC}(t)$ is $n(t)$, which depends strongly on the type of non-geminate recombination mechanism.

At the beginning, we will focus on first order recombination processes, with the following relationship between the recombination rate $R_1(t)$ and the charge carrier density $n(t)$:

$$R_1(t) = \frac{dn(t)}{dt} = -k_1 \cdot n(t), \tag{3}$$

with k_1 as the first order recombination coefficient. Variable separation, integration, and insertion of the boundary conditions then yield:

$$n(t) = n_0 \cdot \exp\{-k_1 \cdot t\}, \tag{4}$$

where n_0 is the initial charge carrier density at $t = 0$. The insertion of Equation (4) into Equation (2) then leads to:

$$V_{OC}(t) = \frac{E_{CT}}{q} - \frac{2k_B T}{q} \ln\left(\frac{N_0}{n_0}\right) \cdot k_1 \cdot t, \tag{5}$$

which allows for the calculation of the time dependence of $V_{OC}(t)$ in the case of first order recombination losses.

The equation describing second order recombination losses can be derived in a similar fashion, starting from the relationship between the recombination rate of second order recombination R_2 and the charge carrier density $n(t)$:

$$R_2(t) = \frac{dn(t)}{dt} = -k_2 \cdot n(t)^2, \tag{6}$$

where k_2 is the recombination coefficient of second order recombination. This time, variable separation, integration, and insertion of the boundary conditions yield:

$$n(t) = \left[k_2 \cdot t + \frac{1}{n_0}\right]^{-1}, \tag{7}$$

with n_0 as the initial charge carrier density. Insertion of Equation (7) into Equation (2) leads to:

$$V_{OC}(t) = \frac{E_{CT}}{q} - \frac{2k_B T}{q} \ln\left(\frac{N_0}{n_0} + N_0 \cdot k_2 \cdot t\right). \tag{8}$$

Finally, the basis for the calculation of the time dependence of $V_{OC}(t)$ for third order recombination is the following relationship:

$$R_3(t) = \frac{dn(t)}{dt} = -k_3 \cdot n(t)^3, \tag{9}$$

where k_3 is the third order recombination coefficient. Once again, variable separation, integration, and insertion of the boundary conditions are employed, leading to:

$$n(t) = \left[2k_3 \cdot t + \frac{1}{n_0^2}\right]^{-0.5}, \tag{10}$$

with n_0 as the initial charge carrier density. Insertion of Equation (10) into Equation (2) yields:

$$V_{OC}(t) = \frac{E_{CT}}{q} - \frac{k_B T}{q} \ln\left(\frac{N_0^2}{n_0^2} + 2N_0^2 \cdot k_3 \cdot t\right). \tag{11}$$

It should be highlighted that the equations derived above are for systems that purely exhibit only one type of non-geminate recombination mechanism. Therefore, they may only act as approximations. Nonetheless, these analytical expressions can be used to calculate and compare the V_{OC}-t-traces of hypothetical devices exhibiting only one type of non-geminate recombination. Thus, they may act as a guideline to quickly gauge experimental data, as we will see later.

To this end, five V_{OC}-t-traces were analytically determined each for first, second, and third order recombination (cf. Figure 2). The initial recombination rates R_0, which are the recombination rates for a given trace $R(t)$ at $t = 0$, were kept at identical values for the five aforementioned traces to enable a better comparison between the first, second, and third order V_{OC}-t-plots, with the only exception being the maximum R_0 values, which did show some variations. The necessary recombination coefficients k_1, k_2, and k_3 to obtain the identical initial recombination rates R_0 were determined in Figure 3 and are listed in Table 1. More details about this calculation can be found in Appendix B. Interestingly,

the initial recombination rates R_0 increase with increasing recombination coefficients, but then reach a maximum and subsequently decrease in value, which can be seen in Figure 3 and for some selected values in the bottom row of Figure 2. However, even though the initial recombination rates R_0 for the same recombination order may be identical, the V_{OC}-t-traces are significantly different owing to the rapidly changing recombination rates $R(t)$ during the decay.

The V_{OC}-t-traces with first order recombination exhibit a linear decrease, which is apparent from Equation (5) (note that the x-axes in Figure 2 are logarithmic). In contrast, the V_{OC}-t-traces with second and third order recombination follow a logarithmic decay. Interestingly, this opens up the possibility to qualitatively determine the order of recombination by determining the slope of V_{OC}-t-traces. To be more precise, the derivative of the open-circuit voltage versus the logarithm of the time $\frac{dV_{OC}(t)}{d\log(t/s)}$ was used, as it is more convenient to work with when using logarithmic x-axes (cf. Figure 2, middle row).

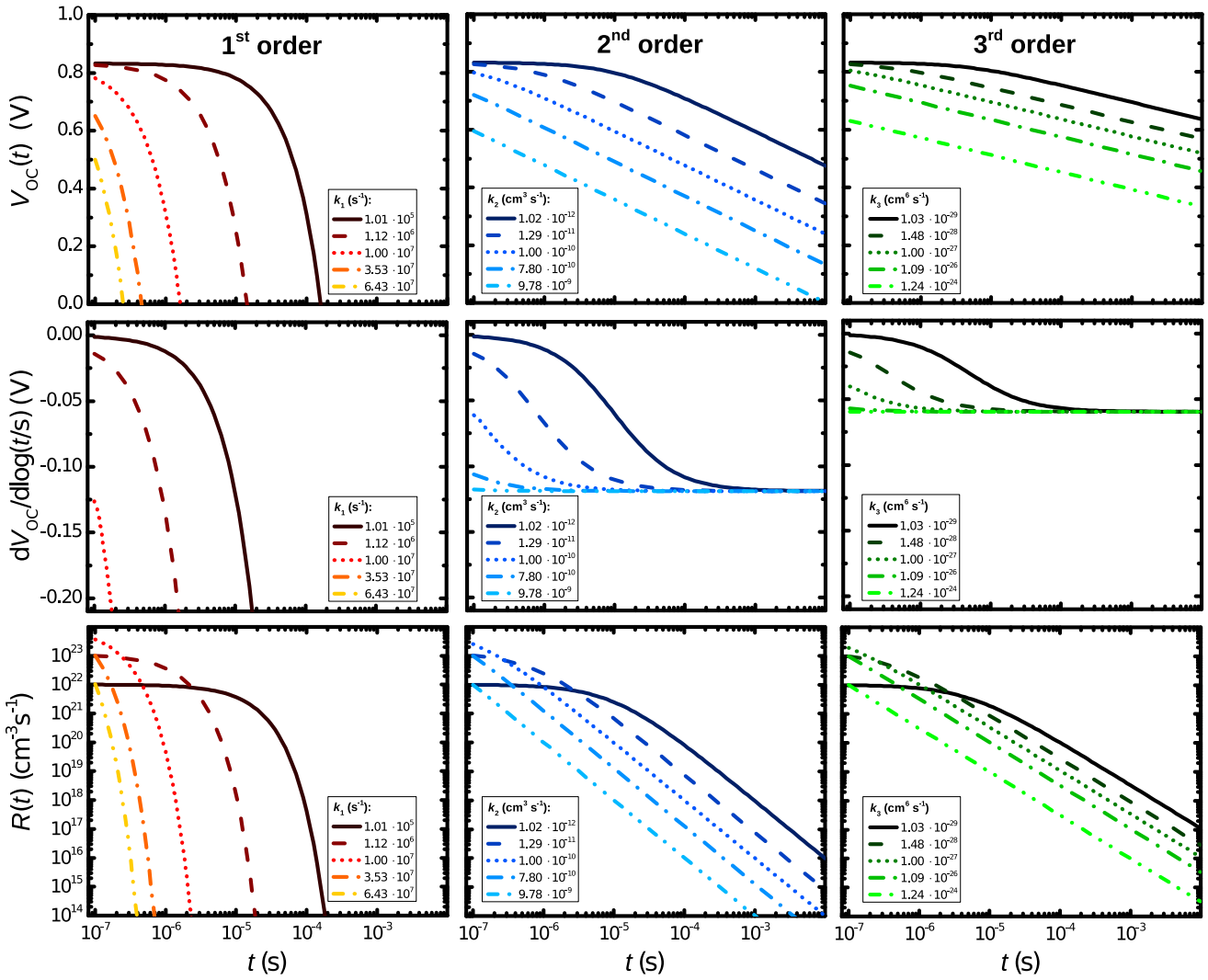

Figure 2. Analytically determined V_{OC}-t-, $dV_{OC}/d\log(t/s)$-t- and R-t-plots for hypothetical solar cells dominated by first, second, or third order recombination, fixed to certain initial recombination rates R_0 for comparison. See Figure 3 and Table 1 for further details.

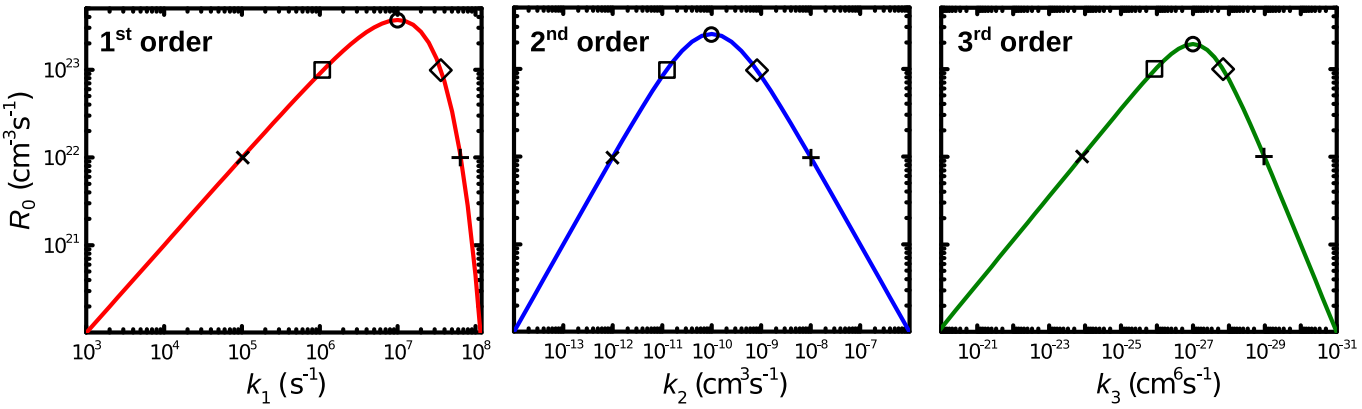

Figure 3. Initial recombination rates R_0 in dependence of the recombination coefficients k_1, k_2, and k_3, calculated following the approach described in Appendix B. The symbols highlight the exact values of R_0 that were used for the calculation of the $V_{OC}(t)$ and $R(t)$ plots depicted in Figure 2 and listed in Table 1.

Table 1. Overview of the different, initial recombination rates R_0 and the underlying recombination coefficients k that were used in Figure 2 and determined in Figure 3. The initial charge carrier density was kept constant at $n_0 = 1 \times 10^{17}$ cm^{-3}.

Symbol	k_1 $\left(\frac{1}{s}\right)$	R_0 $\left(\frac{1}{s \cdot cm^3}\right)$	k_2 $\left(\frac{cm^3}{s}\right)$	R_0 $\left(\frac{1}{s \cdot cm^3}\right)$	k_3 $\left(\frac{cm^6}{s}\right)$	R_0 $\left(\frac{1}{s \cdot cm^3}\right)$
× —	1.0×10^5	1.0×10^{22}	1.0×10^{-12}	1.0×10^{22}	1.0×10^{-29}	1.0×10^{22}
□ - -	1.1×10^6	1.0×10^{23}	1.3×10^{-11}	1.0×10^{23}	1.5×10^{-28}	1.0×10^{23}
◯ ····	1.0×10^7	3.7×10^{23}	1.0×10^{-10}	2.5×10^{23}	1.0×10^{-27}	1.9×10^{23}
◊ —·	3.5×10^7	1.0×10^{23}	7.8×10^{-10}	1.0×10^{23}	1.1×10^{-26}	1.0×10^{23}
+ —··	6.4×10^7	1.0×10^{22}	9.8×10^{-9}	1.0×10^{22}	1.2×10^{-24}	1.0×10^{22}

Unsurprisingly, the slopes of the first order traces decrease continuously. However, the slopes of the second and third order traces converge to approximately -0.13 V and -0.06 V, respectively. Therefore, an analysis of the slope $\frac{dV_{OC}(t)}{d\log(t/s)}$ can yield important qualitative information on the type of recombination, without delving into more complex calculations and analyses that either require certain assumptions or further measurements to obtain the charge carrier density $n(t)$ [29,49]. However, if the recombination coefficients are comparatively small, the convergence only occurs on longer timescales. If one happens to obtain the recombination rates $R(t)$, a similar analysis is possible by determining the slopes $\frac{dR(t)}{d\log(t/s)}$, although such a qualitative analysis is in most cases redundant, as the knowledge of $R(t)$ should already enable the quantitative determination of the various recombination coefficients (k_1, k_2, k_3).

Combinations of several types of non-geminate recombination, such as first/second, second/third, first/third, and first/second/third order, are also possible and more realistic in actual devices. However, the analytical determination of the V_{OC}-t-traces is not always possible, and the reduced forms of the differential equations were determined for completeness and are listed in Appendix C. Nonetheless, the three cases with a single type of non-geminate recombination order can already bestow crucial information, as we will see below with several experimental examples.

3.2. Determination of the Charge Carrier Density

The determination of the time-dependent charge carrier density $n(t)$ is an important prerequisite to obtain quantitative insights with regard to the recombination rates R and recombination coefficients k, as discussed above and in more detail in Section 3.3. The most common approach would be to use a secondary technique other than OCVD to obtain time-dependent values for the charge carrier density. However, there are other strategies that can be used as well. The basis for a quantitative analysis of the V_{OC}-t-traces

is the conversion of the time-dependent open-circuit voltage $V_{OC}(t)$ to the time-dependent charge carrier density $n(t)$ via the following relationship:

$$n(t) = n_i \cdot \exp\left\{\frac{qV_{OC}(t)}{2k_BT}\right\} \quad (12)$$

where n_i is the intrinsic charge carrier density. Since $V_{OC}(t)$ is known from the OCVD measurement, the only missing variable is n_i.

The first strategy is based on the calculation of n_i using estimated values of the effective density of states N_0 and the energy of the charge transfer state E_{CT} via the following relationship:

$$n_i = N_0 \cdot \exp\left\{-\frac{E_{CT}}{2k_BT}\right\}. \quad (13)$$

Typical values for the effective density of states of organic semiconductor blends were given as $N_0 \approx 2.5 \times 10^{19}$ cm^{-3} [55] or could be estimated as the number of repeat units per cubic centimeter in a thin film of a polymer semiconductor. Similarly, E_{CT} can be obtained from the literature for more common blend systems. Otherwise, additional measurements, such as a combination of external quantum efficiency and electroluminescence spectra [53,56] or a combination of temperature and light-intensity-dependent *J*-*V* characteristics [57], are required. However, the method described above is an estimation and should be treated as such.

The second approach focuses on the initial charge carrier density n_0 and initial recombination lifetime τ_0 for a given light intensity:

$$n_0 = \frac{\tau_0 \cdot J_{rec,OC}}{qL}, \quad (14)$$

where $J_{rec,OC}$ is the recombination current density under open-circuit conditions, which can be determined from *J*-*V* curves, q is the elementary charge, and L is the active layer thickness. The initial recombination lifetime τ_0 can be obtained just from the OCVD measurements, as is described at great length in Ref. [49]. A combination of OCVD and *J*-*V* measurements at a single light intensity can already yield n_0, although measurements at several light intensities would be preferable to obtain more reliable results. Once n_0 is known, n_i is accessible through the following relationship:

$$n_i = n_0 \cdot \exp\left\{-\frac{qV_{OC}}{2k_BT}\right\}. \quad (15)$$

Subsequently, the knowledge of n_i enables the conversion of the time-dependent open-circuit voltage $V_{OC}(t)$ to the time-dependent charge carrier density $n(t)$ according to Equation (12).

3.3. Experimental Examples

As mentioned at the end of Section 3.1, three experimental examples have been selected depicting V_{OC}-*t*-traces mainly dominated by either first, second, or third order recombination processes, namely, devices based on PBDBT:CETIC-4F, PM6:Y6, and proton-irradiated $CH_3NH_3PbI_3$ (cf. Figure 4) [29,52,53]. It should be noted that these examples also exhibit other types of recombination that were taken into account to obtain the best fits. The following fundamental equation was necessary to eventually obtain the fitting function:

$$n(t) = n_i \cdot \exp\left\{\frac{qV_{OC}(t)}{2k_BT}\right\} \Leftrightarrow V_{OC}(t) = \frac{2k_BT}{q} \cdot \ln\left[\frac{n(t)}{n_i}\right], \quad (16)$$

where n_i is the intrinsic charge carrier density. Derivation then yields:

$$\frac{\mathrm{d}V_{\mathrm{OC}}(t)}{\mathrm{d}t} = \frac{2k_{\mathrm{B}}T}{q} \cdot \left[\frac{n(t)}{n_i}\right]^{-1} \cdot \frac{1}{n_i} \cdot \frac{\mathrm{d}n(t)}{\mathrm{d}t} = \frac{2k_{\mathrm{B}}T}{q} \cdot \frac{1}{n(t)} \cdot \frac{\mathrm{d}n(t)}{\mathrm{d}t}. \tag{17}$$

In general, it is assumed that the three types of recombination mechanisms discussed so far can occur in parallel without interfering with each other, thus leading to the following superposition of Equations (3), (6), and (9):

$$\frac{\mathrm{d}n(t)}{\mathrm{d}t} = -\Big[k_3 n(t)^3 + k_2 n(t)^2 + k_1 n(t)\Big]. \tag{18}$$

The insertion of Equation (18) into Equation (17) then leads to:

$$\frac{\mathrm{d}V_{\mathrm{OC}}(t)}{\mathrm{d}t} = -\frac{2k_{\mathrm{B}}T}{q} \cdot \Big[k_3 \cdot n(t)^2 + k_2 \cdot n(t) + k_1\Big]. \tag{19}$$

The fitting process itself was carried out on the $\log\left|\frac{\mathrm{d}V_{\mathrm{OC}}(t)}{\mathrm{d}t}\right|$-plots in an effort to put more relative weight on the fitting at shorter timescales (note that the absolute values of the slopes were employed). Therefore, the logarithmic version of Equation (19) was used:

$$\log\left|\frac{\mathrm{d}V_{\mathrm{OC}}(t)}{\mathrm{d}t}\right| = \log\left|-\frac{2k_{\mathrm{B}}T}{q} \cdot \Big[k_3 \cdot n(t)^2 + k_2 \cdot n(t) + k_1\Big]\right|, \tag{20}$$

where the recombination coefficients k_1, k_2, and k_3 were the fitting parameters. The advantage of this approach is the potential to quantitatively determine the recombination coefficients via the fit. However, the necessary prerequisite for the successful fit is the a priori knowledge of the charge carrier density $n(t)$, which can be obtained through independent measurements such as impedance spectroscopy (IS), or a combination of transient photocurrent and transient photovoltage measurements, or via the strategies discussed above in Section 3.2 [47,49]. The charge carrier density was obtained via utilization of IS measurements in the case of the PBDBT:CETIC-4F and PM6:Y6 devices [52,53]. The second strategy discussed in Section 3.2, which is based on the relationship between the recombination current density $J_{\mathrm{rec,OC}}$ and the initial lifetime τ_0, had to be used in the case of the proton-irradiated $CH_3NH_3PbI_3$ solar cell, which is also described in more detail in Ref. [31]. In addition, this strategy was also employed for the PBDBT:CETIC-4F and PM6:Y6 devices, to test the validity of the results and compare them to the IS-based data (cf. Table 2). Indeed, the values for n_0 and n_{i} determined via the two aforementioned approaches are in good agreement for the PBDBT:CETIC-4F device, whereas there are some deviations for the PM6:Y6 device. The use of two different light sources in the measurement setups (IS: solar simulator; OCVD: white LED) can incur deviations. However, it is more likely that the exact approach to determine the charge carrier density via IS has led to overestimated values, which is what is being observed in comparison to the $J_{\mathrm{rec,OC}}$-τ_0-strategy and which has already been described in great detail in Ref. [46].

Be this as it may, it is nonetheless possible to observe that the experimental examples also converge to the $\frac{\mathrm{d}V_{\mathrm{OC}}(t)}{\mathrm{d}\log(t/\mathrm{s})}$-slopes discussed above for the cases of dominant second (-0.13 V) and third (-0.06 V) order recombination, respectively (cf. bottom row of Figure 4). This is very prominent for the irradiated $CH_3NH_3PbI_3$ device and third order recombination, whereas it takes several orders of magnitude for the PM6:Y6 device to converge in the case of second order recombination, which would be expected from a high-performing solar cell exhibiting only limited amounts of (mostly) band-to-band recombination. However, the PM6:Y6 device is then mostly dominated by the continuously decreasing first order recombination on even longer timescales, which only leaves the time span from $t = 1 \times 10^{-5} - 5 \times 10^{-5}$ s, where the convergence is apparent. In the case of the

PBDBT:CETIC-4F, there is no noticeable convergence, which is unsurprising, since it is a device strongly dominated by first order recombination.

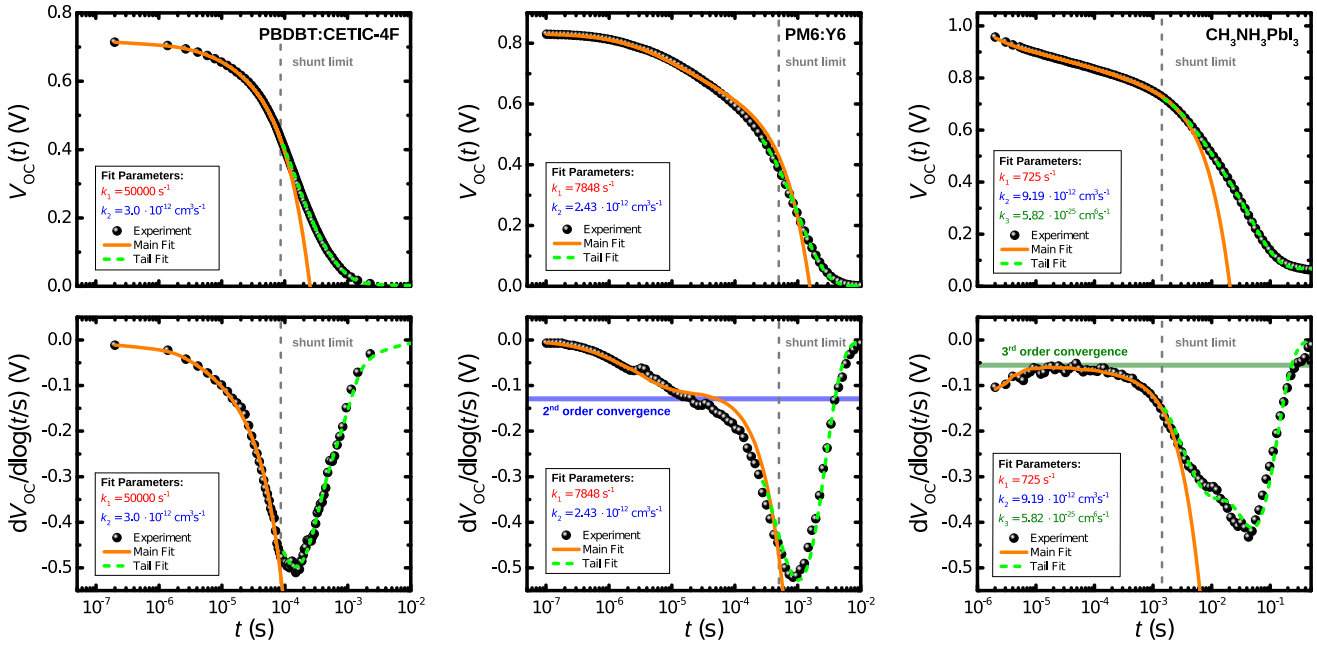

Figure 4. Experimental and fitted V_{OC}-t-traces of devices dominated by first order (PBDBT:CETIC-4F), second order (PM6:Y6), and third order (irradiated $CH_3NH_3PbI_3$) recombination. The main fits (orange lines) are based on Equation (20), whereas the tail fits (green dashes) are based on a mono- (PM6:Y6) or biexponential decay (PBDBT:CETIC-4F; irradiated $CH_3NH_3PbI_3$). The derivatives $dV_{OC}/d\log(t/s)$ are depicted in the bottom row and were essential for the fitting procedure. The parameters for the main fit are the recombination coefficients k_1, k_2, and k_3, which are listed in their respective insets as well as in Table 2. The parameters for the mono- and biexponential decays to fit the tails are also listed in Table 2.

3.4. Deviations between Models and Experiments

However, there are notable differences of the main fits from the experimental examples, though, specifically at longer timescales and smaller $V_{OC}(t)$-values. This is likely related to a breakdown of the model, once the charge carrier density $n(t)$ reaches values under a certain threshold. Thus, the remaining tails of the $V_{OC}(t)$-traces were independently fitted using either a mono- or biexponential decay:

$$V_{OC}(t) = A_1 \cdot \exp\left\{-\frac{t}{\tau_1}\right\} + y_0, \tag{21}$$

$$V_{OC}(t) = A_1 \cdot \exp\left\{-\frac{t}{\tau_1}\right\} + A_2 \cdot \exp\left\{-\frac{t}{\tau_2}\right\} + y_0, \tag{22}$$

where τ is the time constant, A is the exponential prefactor, and y_0 is the offset, respectively (cf. Table 2); this is an approach that has been used in the OCVD measurements of other solar cells [58]. The approach via the exponential decays yields a convincing fit of the tails, as can be seen in Figure 4, most notably when also the derivatives are taken into account. It is striking that the deviations from the recombination model, and thus the start of the tails best described by an exponential decay, can be localized around the extreme point of the slope. Interestingly, this coincides with the timescales that are relevant to leakage and the shunt resistance R_{sh} of the tested solar cells (cf. Figure 4).

Table 2. Overview of the performance, geometric, main fitting, and tail fitting parameters of the three investigated solar cells.

Variable	Device:	PBDBT:CETIC-4F	PM6:Y6	$CH_3NH_3PbI_3$
J_{SC}	($mA \cdot cm^{-2}$)	15.6	25.2	8.7
V_{OC}	(V)	0.71	0.83	0.96
FF	-	0.54	0.74	0.69
η	%	5.96	15.35	5.7
L	(nm)	99.0	90.0	350
A	(cm^2)	0.22	0.22	0.16
C_g	(nF)	6.0	5.6	6.8
ϵ_r	-	3.05	2.58	38
R_{sh}	($\Omega \cdot cm^2$)	2.2×10^4	5.0×10^5	6.0×10^6
t_{sh}	(s)	9.0×10^{-5}	2.5×10^{-4}	1.5×10^{-3}
τ_{RC}	(s)	6.0×10^{-4}	1.3×10^{-2}	2.6×10^{-1}
τ_0	(s)	3.0×10^{-6}	1.4×10^{-6}	1.0×10^{-6}
$n_{0,OCVD}$	(cm^{-3})	3.1×10^{16}	2.5×10^{16}	1.5×10^{15}
$n_{0,IS}$	(cm^{-3})	3.8×10^{16}	2.6×10^{17}	-
$n_{i,OCVD}$	(cm^{-3})	3.1×10^{10}	2.6×10^{9}	8.3×10^{6}
$n_{i,IS}$	(cm^{-3})	3.8×10^{10}	2.1×10^{10}	-
k_1	(s^{-1})	5.0×10^4	7.9×10^3	7.3×10^2
k_2	($cm^3 \cdot s^{-1}$)	3.0×10^{-12}	2.4×10^{-12}	9.2×10^{-12}
k_3	($cm^6 \cdot s^{-1}$)	-	-	5.8×10^{-25}
τ_1	(s)	4.6×10^{-4}	1.0×10^{-3}	5.7×10^{-3}
τ_2	(s)	1.2×10^{-4}	-	5.1×10^{-2}
A_1	(V)	2.7×10^{-1}	6.3×10^{-1}	2.3×10^{-1}
A_2	(V)	4.3×10^{-1}	-	6.5×10^{-3}
y_0	(V)	2.3×10^{-3}	1.0×10^{-3}	6.7×10^{-2}

The shunt resistance of solar cells can be estimated from the differential resistance ($R_{diff} = \frac{\partial V}{\partial J}$) of the device in the dark under short-circuit conditions ($R_{sh} = R_{diff}(0\ V)$) [49]. Once the shunt resistance R_{sh} is equal to the internal resistance R_{in} of the solar cell, it can be assumed that the decay of the open-circuit voltage V_{OC} starts to be dominated by leakage. The internal resistance R_{in} is defined as:

$$R_{in} = \frac{V_{OC}(t)}{J_{in}} = \frac{\tau \cdot V_{OC}(t)}{qL \cdot n(t)}, \tag{23}$$

where J_{in} is the internal current density in the device under open-circuit that is responsible for the loss of charge carriers $n(t)$, either through recombination or leakage mechanisms, where τ is the charge carrier recombination lifetime, q is the elementary charge, and L is the active layer thickness. However, introducing another loss mechanism in the models discussed above should lead to the same or an even faster decay, assuming that the fastest loss channel dominates the process. Although, as the comparison of the fit and the experimental data suggests, the opposite happens, since the overall decay speed decreases significantly.

Another potential explanation for the observed changes in the decay could be related to RC effects of the solar cells, namely, the interplay between the shunt resistance R_{sh} and the geometric capacitance C_g. The characteristic RC time constant τ_{RC} can be determined as follows:

$$\tau_{RC} = \frac{R_{sh} C_g}{A}. \tag{24}$$

It turns out that the time constants τ_{RC} are significantly larger than the time constants from the tail fits τ_1 and τ_2, with the exception of the first order example, where these time

constants are in a similar order of magnitude (cf. Figure 4 and Table 2). Furthermore, the addition of an RC-loss term to the recombination model would also lead to an accelerated decay, rather than a significantly reduced one. Hence, it is likely that the models that successfully describe the different types of non-geminate recombination mechanisms on shorter timescales are simply not valid anymore (cf. Equation (19)).

Moreover, it has been shown that there exists a convergence of V_{OC}-t-traces, when the same device is measured at different light intensities [49]. A full overlap was observed for the V_{OC}-n-traces, which supported the idea of an equivalence between individual V_{OC}-t-measurements at different light intensities and a single V_{OC}-t-measurement at a sufficiently high light intensity. Therefore, the single measurement would encompass all the information about the recombination dynamics as measurements at lower light intensities. This relationship was further confirmed by the identical values determined for the recombination order β, which can also be used to describe the non-geminate recombination dynamics via an effective mechanism:

$$R(t) = \frac{\mathrm{d}n(t)}{\mathrm{d}t} = -k_{\mathrm{eff}} \cdot n(t)^{\beta}. \tag{25}$$

Experimentally, the recombination order β is available via several approaches, first through the second order derivative of the V_{OC}-t-traces:

$$\beta = 1 + \frac{\mathrm{d}\ln\tau^{-1}}{\mathrm{d}\ln n(t)} = 1 + \frac{k_{\mathrm{B}}T}{q} \cdot \frac{\mathrm{d}\ln\tau^{-1}}{\mathrm{d}\ln V_{\mathrm{OC}}(t)}, \tag{26}$$

where τ is the recombination lifetime, defined as:

$$\tau = -\frac{k_{\mathrm{B}}T}{q} \cdot \left(\frac{\mathrm{d}V_{\mathrm{OC}}(t)}{\mathrm{d}t}\right)^{-1}. \tag{27}$$

Then, secondly, via the comparison of the initial charge carrier densities at the beginning of the decay n_0 for V_{OC}-t-traces measured at different light intensities:

$$\tau^{-1} \propto n_0^{\beta-1} \Leftrightarrow \log\tau \propto -(\beta-1)\log n_0. \tag{28}$$

Since there also exists a direct proportionality between the used light intensity and the initial charge carrier density ($I \propto n_0$), one can obtain the recombination order β by determining the slope of a $\log\tau$-$\log I$-plot. Both approaches to obtain the recombination order β typically yield very similar results [49]. Thus, the aforementioned equivalence further supports the hypothesis that the breakdown of the model is related to the charge carrier density $n(t)$ and not simply the time t. Otherwise, one could observe different results, depending on the used light intensity. Another approach is to describe the tail decay based on the time constants that were determined (τ_1, τ_2) either by the de-trapping of charge carriers or polarization effects, which are processes that occur on much longer timescales than non-geminate recombination [59–62]. However, a more detailed investigation is required for a better understanding of the physics behind the tail region of the V_{OC}-t-traces. This particular question should be the focus of future studies though.

4. Conclusions

In conclusion, analytical expressions for first, second, and third order recombination were derived, and the characteristic shapes of hypothetical V_{OC}-t-traces dominated purely by one type of non-geminate recombination were highlighted. The determination of the $\mathrm{d}V_{OC}/\mathrm{d}\log(t/\mathrm{s})$-$t$-plots turned out to be an easily accessible approach to qualitatively inspect the dominant non-geminate recombination process via the convergence of the slopes over time, specifically for second and third order recombination. Moreover, strategies to determine the charge carrier densities were discussed that do not require additional measurements other than OCVD and J-V characteristics. The models resulting from these

analytical expressions were then applied on three different types of solar cells, each of them dominated either by first (PBDBT:CETIC-4F), second (PM6:Y6), or third (irradiated $CH_3NH_3PbI_3$) order recombination, which was clarified by more complex techniques in previous studies. Indeed, the dominant non-geminate recombination process could be determined by simply checking for the convergence of the slopes in the respective $\mathrm{d}V_{\mathrm{OC}}/\mathrm{d}\log(t/\mathrm{s})$-$t$-plots. In addition, deviations from the proposed recombination model and the experimental data at longer timescales caused by the RC circuit, the finite shunt resistance R_{sh}, de-trapping of charge carriers, or polarization effects were also explored.

Author Contributions: J.V. and V.V.B. contributed to methodology, formal analysis, investigation, writing, review and editing. All authors have read and agreed to the published version of the manuscript.

Funding: This research was funded via the Feodor-Lynen Rückkehrstipendium granted to J.V. by the Alexander von Humboldt Stiftung.

Institutional Review Board Statement: Not applicable.

Informed Consent Statement: Not applicable.

Data Availability Statement: Not applicable.

Conflicts of Interest: The authors declare no conflict of interest.

Abbreviations

The following abbreviations are used in this manuscript:

PBDBT	Poly[[4,8-bis[5-(2-ethylhexyl)-2-thienyl]benzo[1,2-b:4,5-b′]dithiophene-2,6-diyl]-2,5-thiophenediyl[5,7-bis(2-ethylhexyl)-4,8-dioxo-4H,8H-benzo-[1,2-c:4,5-c′]dithiophene-1,3-diyl]]
CETIC-4F	Bis(2-ethylhexyl)-2,2′-(4,4-bis(2-ethylhexyl)-4H-cyclopenta[1,2-b:5,4-b′]-dithiophene-2,6-diyl)bis(5-((Z)-(1-(dicyanomethylene)-5,6-difluoro-3-oxo-1H-inden-2(3H)-ylidene)methyl)thiophene-3-carboxylate)
PM6	Poly[[4,8-bis[5-(2-ethylhexyl)-4-fluoro-2-thienyl]benzo[1,2-b:4,5-b′]-dithiophene-2,6-diyl]-2,5-thiophenediyl[5,7-bis(2-ethylhexyl)-4,8-dioxo-4H,8H-benzo[1,2-c:4,5-c′]dithiophene-1,3-diyl]-2,5-thiophenediyl]
Y6	2,2′-((2Z,2′Z)-((12,13-bis(2-ethylhexyl)-3,9-diundecyl-12,13-dihydro-[1,2,5]thiadiazolo[3,4-e]thieno[2″,3″:4′,5′]thieno[2′,3′:4,5]pyrrolo-[3,2-g]thieno[2′,3′:4,5]thieno[3,2-b]indole-2,10-diyl)bis(methanyl-ylidene))bis(5,6-difluoro-3-oxo-2,3-dihydro-1H-indene-2,1-diylidene))dimalononitrile
OCVD	Open-Circuit Voltage Decay
LUMO	Lowest Unoccupied Molecular Orbital
HOMO	Highest Occupied Molecular Orbital
HIB	High Impedance Buffer
IS	Impedance Spectroscopy
V_{OC} (V)	Open-Circuit Voltage
J_{SC} (mA/cm^2)	Short-Circuit Current Density
FF	Fill Factor
η (%)	Power Conversion Efficiency
E_{CT} (eV)	Energy of the Charge Transfer State
q (As)	Elementary Charge
k_{B} (J/K)	Boltzmann's Constant
T (K)	Absolute Temperature
N_0 (cm^{-3})	Effective Density of States
t (s)	Time after Turning Off the Light Source
$n(t)$ (cm^{-3})	Time-Dependent Charge Carrier Density
n_0 (cm^{-3})	Initial Charge Carrier Density at $t = 0$, either via OCVD or IS Approach
n_{i} (cm^{-3})	Intrinsic Charge Carrier Density, either via OCVD or IS Approach
β	Recombination Order ($\beta \approx 1 - 3$)
$R_\beta(t)$ (s^{-1}cm^{-3})	Time-Dependent Recombination Rate of the Order β

R_0 ($s^{-1}cm^{-3}$)	Initial Recombination Rate at $t = 0$
k_1 (s^{-1})	1st Order Recombination Coefficient
k_2 (cm^3/s)	2nd Order Recombination Coefficient
k_3 (cm^6/s)	3rd Order Recombination Coefficient
R_{diff} (Ωcm^2)	Differential Resistance
R_{sh} (Ωcm^2)	Shunt Resistance
R_{in} (Ωcm^2)	Internal Resistance
J_{in} (mA/cm^2)	Internal Current Density
J_{rec} (mA/cm^2)	Recombination Current Density
τ (s)	Recombination Lifetime
τ_0 (s)	Initial Recombination Lifetime at $t = 0$
τ_{RC} (s)	RC Time Constant

Appendix A. Relationship between the Open-Circuit Voltage, Effective Density of States, and Intrinsic Charge Carrier Density

The basis for the analytical expressions of the open-circuit voltage in dependence of time discussed in Section 3.1 (Equation (2)) and Section 3.3 (Equation (16)) are related through the intrinsic charge carrier density n_i, as shown below:

$$V_{OC}(t) = \frac{2k_BT}{q} \cdot \ln\left[\frac{n(t)}{n_i}\right], \tag{A1}$$

where the intrinsic charge carrier density n_i is defined as:

$$n_i = N_0 \cdot \exp\left\{-\frac{E_{CT}}{2k_BT}\right\}. \tag{A2}$$

Insertion of Equation (A2) into Equation (A1) then leads to:

$$V_{OC}(t) = \frac{2k_BT}{q} \cdot \ln\left[\frac{n(t)}{N_0 \cdot \exp\{-\frac{E_{CT}}{2k_BT}\}}\right] = \frac{2k_BT}{q} \cdot \left(\ln[n(t)] - \left[\ln[N_0] - \frac{E_{CT}}{2k_BT}\right]\right). \tag{A3}$$

Simplification of Equation (A3) leads to the familiar expression used in Section 3.1 (Equation (2)):

$$V_{OC}(t) = \frac{E_{CT}}{q} - \frac{2k_BT}{q}\ln\left(\frac{N_0}{n(t)}\right). \tag{A4}$$

Appendix B. Calculation of the Initial Recombination Rate

The initial recombination rate R_0 for first, second, and third order recombination was discussed in Section 3.1, specifically in the context of Figures 2 and 3. To calculate R_0 for the first order case, Equation (4) has to be inserted into Equation (3), yielding:

$$R_0 = -k_1 \cdot n_0 \cdot \exp\{-k_1 \cdot t_0\}. \tag{A5}$$

In the case of second order recombination, Equation (7) has to be inserted into Equation (6), yielding:

$$R_0 = -k_2 \cdot \left[k_2 \cdot t_0 + \frac{1}{n_0}\right]^{-2}. \tag{A6}$$

To calculate R_0 for the third order case, Equation (10) has to be inserted into Equation (9), yielding:

$$R_0 = -k_3 \cdot \left[2k_3 \cdot t_0 + \frac{1}{n_0^2}\right]^{-1.5}. \tag{A7}$$

To obtain the plots depicted in Figure 3, the recombination coefficients k were varied, whereas the initial charge carrier density ($n_0 = 1 \times 10^{17}$ cm^{-3}) and the initial time ($t_0 = 1 \times 10^{-7}$ s) were kept constant.

Appendix C. Analytical Determination of Combined Recombination Mechanisms

The analytical determination of the V_{OC}-t-traces presented in Section 3.1 is not always possible for all combinations of non-geminate recombination mechanisms. Therefore, the reduced forms of the differential equations were determined for completeness, which are listed below:

$$R_{1,2}(t) = \frac{\mathrm{d}n(t)}{\mathrm{d}t} = -\Big(k_2 \cdot n(t)^2 + k_1 \cdot n(t)\Big), \tag{A8}$$

$$n_{1,2}(t) = -\frac{k_1 \cdot \exp\{-k_1 \cdot \gamma\}}{k_2 \cdot \exp\{-k_1 \cdot \gamma\} - \exp\{-k_1 \cdot t\}}, \tag{A9}$$

$$R_{2,3}(t) = \frac{\mathrm{d}n(t)}{\mathrm{d}t} = -\Big(k_3 \cdot n(t)^3 + k_2 \cdot n(t)^2\Big), \tag{A10}$$

$$\gamma - t = -\frac{k_3 \cdot \ln[n_{2,3}(t)]}{k_2^2} + \frac{k_3 \cdot \ln[k_3 \cdot n_{2,3}(t) + k_2]}{k_2^2} - \frac{1}{k_2 \cdot n_{2,3}(t)}, \tag{A11}$$

$$R_{1,3}(t) = \frac{\mathrm{d}n(t)}{\mathrm{d}t} = -\Big(k_3 \cdot n(t)^3 + k_1 \cdot n(t)\Big), \tag{A12}$$

$$n_{1,3}(t) = \pm\sqrt{\frac{k_1}{\exp\{2k_1 \cdot (\gamma + 1) - k_3)\}}}, \tag{A13}$$

$$R_{1,2,3}(t) = \frac{\mathrm{d}n(t)}{\mathrm{d}t} = -\Big(k_3 \cdot n(t)^3 + k_2 \cdot n(t)^2 + k_1 \cdot n(t)\Big), \tag{A14}$$

$$\gamma - t = \frac{\frac{2k_2 \tan^{-1}\left(\frac{2k_3 n_{1,2,3}(t) + k_2}{\sqrt{4k_3k_1 - k_2^2}}\right)}{\sqrt{4k_3k_1 - k_2^2}} + \ln[n_{1,2,3}(t) \cdot (k_3 n_{1,2,3}(t) + k_2) + k_1] - 2\ln[n_{1,2,3}(t)]}{2k_1}, \tag{A15}$$

where $R(t)$ is the recombination rate, k is the relevant recombination coefficient, t is the time, $n(t)$ is the transient charge carrier density of the various cases, and where γ is a constant resulting from the integration.

References

1. Bui, T.T.; Goubard, F.; Ibrahim-Ouali, M.; Gigmes, D.; Dumur, F. Thermally Activated Delayed Fluorescence Emitters for Deep Blue Organic Light Emitting Diodes: A Review of Recent Advances. *Appl. Sci.* **2018**, *8*, 494. [CrossRef]
2. Kalyani, N.T.; Dhoble, S. Organic light emitting diodes: Energy saving lighting technology—A review. *Renew. Sustain. Energy Rev.* **2012**, *16*, 2696–2723. [CrossRef]
3. Van Le, Q.; Jang, H.W.; Kim, S.Y. Recent Advances toward High-Efficiency Halide Perovskite Light-Emitting Diodes: Review and Perspective. *Small Methods* **2018**, *2*, 1700419. [CrossRef]
4. Vollbrecht, J.; Wiebeler, C.; Bock, H.; Schumacher, S.; Kitzerow, H.S. Curved Polar Dibenzocoronene Esters and Imides versus Their Planar Centrosymmetric Homologs: Photophysical and Optoelectronic Analysis. *J. Phys. Chem. C* **2019**, *123*, 4483–4492. [CrossRef]
5. Lill, A.T.; Cao, D.X.; Schrock, M.; Vollbrecht, J.; Huang, J.; Nguyen-Dang, T.; Brus, V.V.; Yurash, B.; Leifert, D.; Bazan, G.C.; et al. Organic Electrochemical Transistors Based on the Conjugated Polyelectrolyte PCPDTBT-SO3K (CPE-K). *Adv. Mater.* **2020**, *32*, 1908120. [CrossRef] [PubMed]
6. Sirringhaus, H. 25th Anniversary Article: Organic Field-Effect Transistors: The Path Beyond Amorphous Silicon. *Adv. Mater.* **2014**, *26*, 1319–1335. [CrossRef]
7. Surya, S.G.; Raval, H.N.; Ahmad, R.; Sonar, P.; Salama, K.N.; Rao, V.R. Organic field effect transistors (OFETs) in environmental sensing and health monitoring: A review. *TrAC Trends. Anal. Chem.* **2019**, *111*, 27–36. [CrossRef]
8. Vollbrecht, J.; Oechsle, P.; Stepen, A.; Hoffmann, F.; Paradies, J.; Meyers, T.; Hilleringmann, U.; Schmidtke, J.; Kitzerow, H. Liquid crystalline dithienothiophene derivatives for organic electronics. *Org. Electron.* **2018**, *61*, 266–275. [CrossRef]
9. Brus, V.V.; Lee, J.; Luginbuhl, B.R.; Ko, S.J.; Bazan, G.C.; Nguyen, T.Q. Solution-Processed Semitransparent Organic Photovoltaics: From Molecular Design to Device Performance. *Adv. Mater.* **2019**, *31*, 1900904. [CrossRef]

10. Wadsworth, A.; Moser, M.; Marks, A.; Little, M.S.; Gasparini, N.; Brabec, C.J.; Baran, D.; McCulloch, I. Critical review of the molecular design progress in non-fullerene electron acceptors towards commercially viable organic solar cells. *Chem. Soc. Rev.* **2019**, *48*, 1596–1625. [CrossRef]
11. Hu, Z.; Wang, J.; Ma, X.; Gao, J.; Xu, C.; Yang, K.; Wang, Z.; Zhang, J.; Zhang, F. A critical review on semitransparent organic solar cells. *Nano Energy* **2020**, 105376. [CrossRef]
12. Lee, J.; Ko, S.J.; Lee, H.; Huang, J.; Zhu, Z.; Seifrid, M.; Vollbrecht, J.; Brus, V.V.; Karki, A.; Wang, H.; et al. Side-Chain Engineering of Nonfullerene Acceptors for Near-Infrared Organic Photodetectors and Photovoltaics. *ACS Energy Lett.* **2019**, *4*, 1401–1409. [CrossRef]
13. Pecunia, V. Efficiency and spectral performance of narrowband organic and perovskite photodetectors: A cross-sectional review. *J. Phys. Mater.* **2019**, *2*, 042001. [CrossRef]
14. Tang, X.; Matt, G.J.; Gao, S.; Gu, E.; Almora, O.; Brabec, C.J. Electrical-Field-Driven Tunable Spectral Responses in a Broadband-Absorbing Perovskite Photodiode. *ACS Appl. Mater. Interfaces* **2019**, *11*, 39018–39025. [CrossRef] [PubMed]
15. Huang, J.; Lee, J.; Vollbrecht, J.; Brus, V.V.; Dixon, A.L.; Cao, D.X.; Zhu, Z.; Du, Z.; Wang, H.; Cho, K.; et al. A High-Performance Solution-Processed Organic Photodetector for Near-Infrared Sensing. *Adv. Mater.* **2020**, *32*, 1906027. [CrossRef]
16. Yeo, S.Y.; Park, S.; Yi, Y.J.; Kim, D.H.; Lim, J.A. Highly Sensitive Flexible Pressure Sensors Based on Printed Organic Transistors with Centro-Apically Self-Organized Organic Semiconductor Microstructures. *ACS Appl. Mater. Interfaces* **2017**, *9*, 42996–43003. [CrossRef]
17. Pappa, A.M.; Parlak, O.; Scheiblin, G.; Mailley, P.; Salleo, A.; Owens, R.M. Organic Electronics for Point-of-Care Metabolite Monitoring. *Trends. Biotechnol.* **2018**, *36*, 45–59. [CrossRef]
18. Pudzs, K.; Vembris, A.; Rutkis, M.; Woodward, S. Thin Film Organic Thermoelectric Generator Based on Tetrathiotetracene. *Adv. Electron. Mater.* **2017**, *3*, 1600429. [CrossRef]
19. Huang, J.; Karki, A.; Brus, V.V.; Hu, Y.; Phan, H.; Lill, A.T.; Wang, M.; Bazan, G.C.; Nguyen, T.Q. Solution-Processed Ion-Free Organic Ratchets with Asymmetric Contacts. *Adv. Mater.* **2018**, *30*, 1804794. [CrossRef]
20. Hao, J.; Lu, H.; Nanayakkara, S.U.; Harvey, S.P.; Blackburn, J.L.; Ferguson, A.J. Perovskite Electronic Ratchets for Energy Harvesting. *Adv. Electron. Mater.* **2020**, *6*, 2000831. [CrossRef]
21. Roy, P.; Sinha, N.K.; Tiwari, S.; Khare, A. A review on perovskite solar cells: Evolution of architecture, fabrication techniques, commercialization issues and status. *Sol. Energy* **2020**, *198*, 665–688. [CrossRef]
22. Li, N.; Niu, X.; Chen, Q.; Zhou, H. Towards commercialization: The operational stability of perovskite solar cells. *Chem. Soc. Rev.* **2020**, *49*, 8235–8286. [CrossRef]
23. Riede, M.; Spoltore, D.; Leo, K. Organic Solar Cells—The Path to Commercial Success. *Adv. Energy Mater.* **2021**, *11*, 2002653. [CrossRef]
24. Darling, S.B.; You, F. The case for organic photovoltaics. *RSC Adv.* **2013**, *3*, 17633–17648. [CrossRef]
25. Guo, J.; Min, J. A Cost Analysis of Fully Solution-Processed ITO-Free Organic Solar Modules. *Adv. Energy Mater.* **2019**, *9*, 1802521. [CrossRef]
26. Credgington, D.; Jamieson, F.C.; Walker, B.; Nguyen, T.Q.; Durrant, J.R. Quantification of Geminate and Non-Geminate Recombination Losses within a Solution-Processed Small-Molecule Bulk Heterojunction Solar Cell. *Adv. Mater.* **2012**, *24*, 2135–2141. [CrossRef] [PubMed]
27. Shockley, W.; Read, W., Jr. Statistics of the Recombinations of Holes and Electrons. *Phys. Rev.* **1952**, *87*, 835. [CrossRef]
28. Koster, L.; Mihailetchi, V.; Blom, P. Bimolecular recombination in polymer/fullerene bulk heterojunction solar cells. *Appl. Phys. Lett.* **2006**, *88*, 052104. [CrossRef]
29. Brus, V.V.; Lang, F.; Bundesmann, J.; Seidel, S.; Denker, A.; Rech, B.; Landi, G.; Neitzert, H.C.; Rappich, J.; Nickel, N.H. Defect Dynamics in Proton Irradiated CH3NH3PbI3 Perovskite Solar Cells. *Adv. Electron. Mater.* **2017**, *3*, 1600438. [CrossRef]
30. Göhler, C.; Wagenpfahl, A.; Deibel, C. Nongeminate Recombination in Organic Solar Cells. *Adv. Electron. Mater.* **2018**, *4*, 1700505. [CrossRef]
31. Vollbrecht, J.; Brus, V.V. On the recombination order of surface recombination under open circuit conditions. *Org. Electron.* **2020**, *86*, 105905. [CrossRef]
32. Brus, V.V. Light dependent open-circuit voltage of organic bulk heterojunction solar cells in the presence of surface recombination. *Org. Electron.* **2016**, *29*, 1–6. [CrossRef]
33. Yang, C.; Zhang, J.; Liang, N.; Yao, H.; Wei, Z.; He, C.; Yuan, X.; Hou, J. Effects of energy-level offset between a donor and acceptor on the photovoltaic performance of non-fullerene organic solar cells. *J. Mater. Chem. A* **2019**, *7*, 18889–18897. [CrossRef]
34. McDowell, C.; Abdelsamie, M.; Toney, M.F.; Bazan, G.C. Solvent Additives: Key Morphology-Directing Agents for Solution-Processed Organic Solar Cells. *Adv. Mater.* **2018**, *30*, 1707114. [CrossRef] [PubMed]
35. Shi, M.; Wang, T.; Sun, R.; Wu, Q.; Pei, D.; Wang, H.; Yang, W.; Wang, W.; Wu, Y.; Xie, G.; et al. Remove the water-induced traps toward improved performance in organic solar cells. *Sci. China Mater.* **2021**, 1–16. [CrossRef]
36. Schwarz, K.N.; Geraghty, P.B.; Jones, D.J.; Smith, T.A.; Ghiggino, K.P. Suppressing Subnanosecond Bimolecular Charge Recombination in a High-Performance Organic Photovoltaic Material. *J. Phys. Chem. C* **2016**, *120*, 24002–24010. [CrossRef]
37. Yi, Z.; Ni, W.; Zhang, Q.; Li, M.; Kan, B.; Wan, X.; Chen, Y. Effect of thermal annealing on active layer morphology and performance for small molecule bulk heterojunction organic solar cells. *J. Mater. Chem. C* **2014**, *2*, 7247–7255. [CrossRef]

38. Bonasera, A.; Giuliano, G.; Arrabito, G.; Pignataro, B. Tackling performance challenges in organic photovoltaics: An overview about compatibilizers. *Molecules* **2020**, *25*, 2200. [CrossRef] [PubMed]
39. Hoefler, S.F.; Rath, T.; Pastukhova, N.; Pavlica, E.; Scheunemann, D.; Wilken, S.; Kunert, B.; Resel, R.; Hobisch, M.; Xiao, S.; et al. The effect of polymer molecular weight on the performance of PTB7-Th: O-IDTBR non-fullerene organic solar cells. *J. Mater. Chem. A* **2018**, *6*, 9506–9516. [CrossRef]
40. Karki, A.; Vollbrecht, J.; Gillett, A.J.; Xiao, S.S.; Yang, Y.; Peng, Z.; Schopp, N.; Dixon, A.L.; Yoon, S.; Schrock, M.; et al. The role of bulk and interfacial morphology in charge generation, recombination, and extraction in non-fullerene acceptor organic solar cells. *Energy Environ. Sci.* **2020**, *13*, 3679–3692. [CrossRef]
41. Yao, J.; Qiu, B.; Zhang, Z.G.; Xue, L.; Wang, R.; Zhang, C.; Chen, S.; Zhou, Q.; Sun, C.; Yang, C.; et al. Cathode engineering with perylene-diimide interlayer enabling over 17% efficiency single-junction organic solar cells. *Nat. Commun.* **2020**, *11*, 1–10. [CrossRef] [PubMed]
42. Brus, V.V.; Lee, H.K.; Proctor, C.M.; Ford, M.; Liu, X.; Burgers, M.A.; Lee, J.; Bazan, G.C.; Nguyen, T.Q. Balance Between Light Absorption and Recombination Losses in Solution-Processed Small Molecule Solar Cells with Normal or Inverted Structures. *Adv. Energy Mater.* **2018**, *8*, 1801807. [CrossRef]
43. Koster, L.J.A.; Mihailetchi, V.; Xie, H.; Blom, P.W. Origin of the light intensity dependence of the short-circuit current of polymer/fullerene solar cells. *Appl. Phys. Lett.* **2005**, *87*, 203502. [CrossRef]
44. Koster, L.J.A.; Mihailetchi, V.D.; Ramaker, R.; Blom, P.W. Light intensity dependence of open-circuit voltage of polymer: Fullerene solar cells. *Appl. Phys. Lett.* **2005**, *86*, 123509. [CrossRef]
45. Cowan, S.R.; Banerji, N.; Leong, W.L.; Heeger, A.J. Charge Formation, Recombination, and Sweep-Out Dynamics in Organic Solar Cells. *Adv. Funct. Mater.* **2012**, *22*, 1116–1128. [CrossRef]
46. Vollbrecht, J.; Brus, V.V. On Charge Carrier Density in Organic Solar Cells Obtained via Capacitance Spectroscopy. *Adv. Electron. Mater.* **2020**, *6*, 2000517. [CrossRef]
47. Brus, V.V.; Proctor, C.M.; Ran, N.A.; Nguyen, T.Q. Capacitance Spectroscopy for Quantifying Recombination Losses in Non-fullerene Small-Molecule Bulk Heterojunction Solar Cells. *Adv. Energy Mater.* **2016**, *6*, 1502250. [CrossRef]
48. Nakano, K.; Chen, Y.; Tajima, K. Quantifying charge carrier density in organic solar cells by differential charging techniques. *AIP Adv.* **2019**, *9*, 125205. [CrossRef]
49. Vollbrecht, J.; Brus, V.V.; Ko, S.J.; Lee, J.; Karki, A.; Cao, D.X.; Cho, K.; Bazan, G.C.; Nguyen, T.Q. Quantifying the Nongeminate Recombination Dynamics in Nonfullerene Bulk Heterojunction Organic Solar Cells. *Adv. Energy Mater.* **2019**, *9*, 1901438. [CrossRef]
50. Elliott, L.C.; Basham, J.I.; Pernstich, K.P.; Shrestha, P.R.; Richter, L.J.; DeLongchamp, D.M.; Gundlach, D.J. Probing Charge Recombination Dynamics in Organic Photovoltaic Devices under Open-Circuit Conditions. *Adv. Energy Mater.* **2014**, *4*, 1400356. [CrossRef]
51. Phuong, L.Q.; Hosseini, S.M.; Sandberg, O.J.; Zou, Y.; Woo, H.Y.; Neher, D.; Shoaee, S. Quantifying Quasi-Fermi Level Splitting and Open-Circuit Voltage Losses in Highly Efficient Nonfullerene Organic Solar Cells. *Sol. RRL* **2021**, *5*, 2000649. [CrossRef]
52. Vollbrecht, J.; Lee, J.; Ko, S.J.; Brus, V.V.; Karki, A.; Le, W.; Seifrid, M.; Ford, M.J.; Cho, K.; Bazan, G.C.; et al. Design of narrow bandgap non-fullerene acceptors for photovoltaic applications and investigation of non-geminate recombination dynamics. *J. Mater. Chem. C* **2020**, *8*, 15175–15182. [CrossRef]
53. Karki, A.; Vollbrecht, J.; Dixon, A.L.; Schopp, N.; Schrock, M.; Reddy, G.M.; Nguyen, T.Q. Understanding the High Performance of over 15% Efficiency in Single-Junction Bulk Heterojunction Organic Solar Cells. *Adv. Mater.* **2019**, *31*, 1903868. [CrossRef] [PubMed]
54. Neukom, M.; Züfle, S.; Jenatsch, S.; Ruhstaller, B. Opto-electronic characterization of third-generation solar cells. *Sci. Technol. Adv. Mater.* **2018**, *19*, 291–316. [CrossRef]
55. Blom, P.W.; De Jong, M.; Vleggaar, J. Electron and hole transport in poly (p-phenylene vinylene) devices. *Appl. Phys. Lett.* **1996**, *68*, 3308–3310. [CrossRef]
56. Armin, A.; Zarrabi, N.; Sandberg, O.J.; Kaiser, C.; Zeiske, S.; Li, W.; Meredith, P. Limitations of Charge Transfer State Parameterization Using Photovoltaic External Quantum Efficiency. *Adv. Energy Mater.* **2020**, *10*, 2001828. [CrossRef]
57. Karki, A.; Vollbrecht, J.; Gillett, A.J.; Selter, P.; Lee, J.; Peng, Z.; Schopp, N.; Dixon, A.L.; Schrock, M.; Nádaždy, V.; et al. Unifying Charge Generation, Recombination, and Extraction in Low-Offset Non-Fullerene Acceptor Organic Solar Cells. *Adv. Energy Mater.* **2020**, *10*, 2001203. [CrossRef]
58. Sakata, I.; Hayashi, Y. Open-circuit voltage decay (OCVD) measurement applied to hydrogenated amorphous silicon solar cells. *Jpn. J. Appl. Phys.* **1990**, *29*, L27. [CrossRef]
59. Brus, V.V.; Lang, F.; Fengler, S.; Dittrich, T.; Rappich, J.; Nickel, N.H. Doping Effects and Charge-Transfer Dynamics at Hybrid Perovskite/Graphene Interfaces. *Adv. Mater. Interfaces* **2018**, *5*, 1800826. [CrossRef]
60. Fu, F.; Kranz, L.; Yoon, S.; Löckinger, J.; Jäger, T.; Perrenoud, J.; Feurer, T.; Gretener, C.; Buecheler, S.; Tiwari, A.N. Controlled growth of PbI2 nanoplates for rapid preparation of CH3NH3PbI3 in planar perovskite solar cells. *Phys. Status Solidi A Appl. Mater.* **2015**, *212*, 2708–2717. [CrossRef]
61. Volonakis, G.; Giustino, F. Ferroelectric Graphene–Perovskite Interfaces. *J. Phys. Chem. Lett.* **2015**, *6*, 2496–2502. [CrossRef] [PubMed]
62. Dang, V.Q.; Han, G.S.; Trung, T.Q.; Jin, Y.U.; Hwang, B.U.; Jung, H.S.; Lee, N.E. Methylammonium lead iodide perovskite-graphene hybrid channels in flexible broadband phototransistors. *Carbon* **2016**, *105*, 353–361. [CrossRef]